Portable High-Accuracy Wireless Acquisition System for Graphene-Based Sensors

Giorgio Biagetti, *Member, IEEE*, Paolo Crippa, *Senior Member, IEEE*, Michele Alessandrini, and Daniele Di Marino

***Abstract*—Graphene-based field-effect transistors (gFETs) are gaining popularity for the realization of biological sensors as their graphene active area provides a convenient basis for attaching organic substances, such as appropriately engineered receptors. The presence of a particular biological agent then translates in the modification of the electrical characteristics of the gFET. We thus developed a compact, portable system that is able to accurately measure those electrical characteristics with high accuracy, by automatically compensating its own offsets and errors. The acquisition device we here present is able to measure drain currents with a nominal accuracy of 0.1% and with an rms noise as low as 22 pA, up to a maximum of 125 μA (22 bits effective resolution), and gFET channel resistances with a nominal accuracy of 0.01% ± 0.1 Ω and with an rms noise as low as 2.13 μV in the range from 100 Ω to 1 MΩ. Due to its performance, small dimensions, and long battery life, it can be used both for scientific research, where portability and ease of use are key features when operating in potentially hazardous environments due to the presence of biological agents, and as a fully automated detector when coupled with the appropriate sensor, as it can perform thousands of measures on a single battery charge and be completely remotely controlled over a Bluetooth low energy (BLE) connection.**

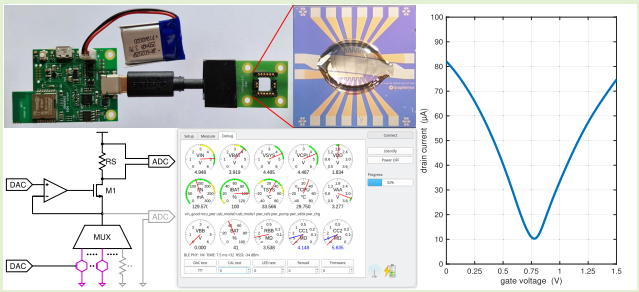

***Index Terms*— Bluetooth sensor, graphene sensor, portable measurement system, readout circuit, source measure unit (SMU), wireless sensor.**

I. Introduction

SENSORS based on field-effect transistors (FETs) have demonstrated attractive features such as small weight and size, integrability, ease of manufacturing, and low production costs. In the past years, many FET-based biosensors exploiting 1-D and 2-D nanomaterials for the transistor channel (e.g., silicon nanowires, carbon nanotubes, transition metal dicalcogenides, and graphene) have been implemented for the detection of various classes of substances in gases and liquids [1], [2], [3].

Manuscript received 3 March 2023; revised 17 April 2023; accepted 26 May 2023. Date of publication 5 June 2023; date of current version 1 August 2023. This work was supported in part by the FISR2020 Program through the Italian Ministry of Research under Grant 03475. The associate editor coordinating the review of this article and approving it for publication was Prof. Boby George. *(Corresponding author: Giorgio Biagetti.)*

Giorgio Biagetti, Paolo Crippa, and Michele Alessandrini are with the Department of Information Engineering, Università Politecnica delle Marche, Ancona, 60131 Ancona, Italy (e-mail: g.biagetti@univpm.it; p.crippa@univpm.it; m.alessandrini@univpm.it).

Daniele Di Marino is with the Department of Life and Environmental Sciences, Università Politecnica delle Marche, Ancona, 60131 Ancona, Italy (e-mail: d.dimarino@univpm.it).

Digital Object Identifier 10.1109/JSEN.2023.3281156

Graphene is a 2-D sheet of hexagonally arranged carbon atoms, all of which are exposed on its surface. It has demonstrated to be a useful material for various sensing platforms due to its extraordinary properties, such as high carrier mobility and high electronic conductivity [4]. In particular, with the development of graphene-based field-effect transistors (gFETs), new possibilities arose for the realization of biological or similar sensing devices as graphene is apt to being easily functionalized for the detection of different biological substances [5], [6], [7], [8], [9], [10], [11], [12], [13], [14], [15], [16]. As a result, gFET biosensors can detect the changes on the transistor surface and provide an optimal sensing environment for very sensitive detection [17], [18]. Considering the pandemic situation of the last couple of years, the gFET technology has been demonstrated to be very attractive for applications related to sensitive diagnosis of COVID-19 or other coronavirus-induced infections [19], [20], [21].

But to be able to actually exploit such capabilities on the field, compact, portable, and possibly wireless acquisition systems are useful [22]. More recently, in [23] a portable, multiplexed, wireless electrochemical platform for ultrarapid detection of COVID-19 was proposed. This platform, called

SARS-CoV-2 RapidPlex, uses capture antigens and antibodies immobilized on mass-producible, low-cost, laser-engraved graphene electrodes for quantitatively detecting biomarkers specific to COVID-19 in both saliva and blood within physiologically significant ranges.

Similarly, in [24] a genosensor exploiting graphene as a working electrode due to its favorable properties, and the streptavidin–biotin interaction to immobilize a capture DNA probe due to their high affinity, was presented. The graphene electrode was embedded into a flexible printed circuit board for the rapid, sensitive, amplification-free, and label-free detection of SARS-CoV-2.

The present article focuses on the development, design, and characterization of a portable wireless system specifically optimized for the acquisition of the electrical characteristics of gFET transistors used as biological sensors. Its main components are the acquisition device proper and the user interface (UI) software. The former is a miniaturized, portable, 12-channel acquisition device that is able to accurately measure the I–V relationships of multiple gFETs, like those found on a Graphenea GFET-S20 sensing element, which consists in 12 liquid-gated gFETs arranged in a common-source configuration with independent drain contacts. The software allows complete remote control of the sensor through a Bluetooth low energy (BLE) connection, chosen because it is already readily available in practically any modern laptop or tablet, and a user-friendly interface helps in performing measures, showing real-time results, and storing the acquired data and calibration reports for long-term archival and/or further processing on a PC. The GFET-S20 sensing element is then connected to the acquisition device through a small, inexpensive, and easily replaceable pod that, in this first prototype version, connects to the graphene chip with matching spring-loaded contacts, and to the acquisition device via its waterproof Type-C USB connector. This arrangement allows great flexibility in the design of the pod, as it can be easily customized to different sensor configurations. Finally, as an application example, the device has been used in a proof-of-concept system for a novel type of COVID-19 virus detector [25].

Several challenges needed to be overcome to design and build such a device. The first one is due to the peculiar operation of gFET devices used for biological sensing. Unlike ordinary FETs, they use liquid-gating, so that the biological agent to be detected is carried within the gating solution. But to avoid electrochemical reactions in the liquid, very low voltages are usually applied. Drain–source biasing voltages should be in the range of tens of millivolts, with 50 mV being a common choice, though lower values can sometimes be asked for. gFETs are also ambipolar devices [26], meaning that their transfer characteristic exhibits a minimum in correspondence to a defined gate–source voltage, called the Dirac point, usually in the 0.5–1.0 V range. When the device is functionalized to detect a particular agent, engineered molecules that are able to attach to the graphene surface on one side, and to the agent to be detected on the other side, are attached to the gFET. When they also attach to the target agent, if present/added to the gating solution, the electrical charge distribution at the transistor surface is changed, resulting in a shift of the Dirac point, which is the telltale of the presence of the agent. Full details of the biochemical process that underlies the detector are given in [25], but for the readout circuit design, the important information is that the shift can be of just a few millivolts. With drain currents of a few microamperes, accurately locating the Dirac point is a challenging task that requires high-resolution and well-calibrated instruments.

The system we present in this article had indeed been optimized for this task. It was specifically built to aid in the experimentation of novel functionalization processes [27] for gFET devices, so we tried to maximize its resolution and accuracy within the constraints of portability, small form factor, and cost. Our prototype device is a 16-cm^2 electronic board that draws less than 65 mW of power while measuring and has a 31-bit ADC with an effective resolution of 22 bits. For comparison, a device that offers somewhat similar functionalities and exploits the same sensing gFET chips was recently presented in [28]. Though the effective resolution is not specified, it uses 16-bit ADCs, it is orders of magnitude bigger and draws more than 1 W of power, and is definitely not wireless, hindering its usage in high-hazardous environments.

This article is structured as follows. Section II describes the structure and detailed operation of the acquisition device, while Section III deals with the customized BLE-based data transmission we implemented, and Section IV describes the UI that controls the whole system. Section V reports on the experimental validation of the system and calibration algorithms. Finally, Section VI concludes this work.

II. Acquisition Device

The behavior of the acquisition device should be that of a controllable voltage source with current metering capabilities, a so-called source measure unit (SMU). The main challenges in the design of a compact, battery-powered, and energy-efficient SMU lie in the low magnitude of the currents that should be measured, from a few nanoamperes to several microamperes, and with a low driving voltage, few millivolts, so as not to alter the electrochemical properties of the gating solution.

The basic current sensing technique is based on an op-amp realization of a current conveyor (CCII), as shown in Fig. 1, where we also highlighted the DAC used to control the gFET drain voltage, the multiplexer (MUX) used to select the sensing channel to be activated, the sensing resistor RS, and the ADC. A secondary (grayed) ADC channel can be used to monitor the drain voltage and thus perform system calibration, as will be discussed in Section II-C, possibly with the help of optional precision calibration resistors connected to spare MUX channels. Finally, another DAC provides the gate voltage to the graphene transistors (shown in purple).

A prototype implementation of the system can be seen in Fig. 2, where a picture of the fully assembled PCB is shown with the portions devoted to power management, the input signal chain (comprising references, current conveyor, and ADC), the MUXs, and the biasing DACs, highlighted, respectively, in red, azure, orange, and purple. The whole

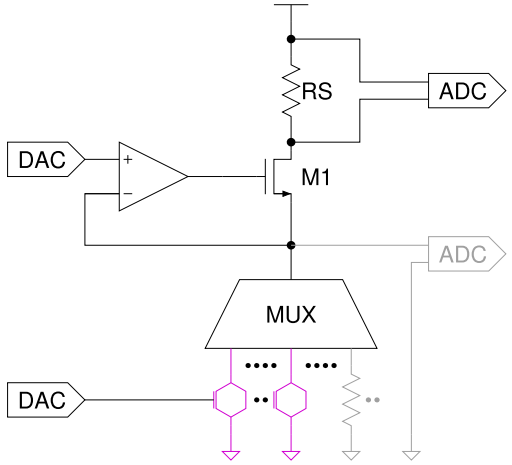

Fig. 1. Basic current sensing technique used by the device. The upper DAC sets the drain voltage, the bottom one sets the gate voltage, while the main ADC senses the drain current. A secondary (gray) ADC allows in-system calibration. The 16-channel MUX allows the selection of 12 individual gFETs (in purple) to be measured, or the connection of up to four calibration resistors (in gray).

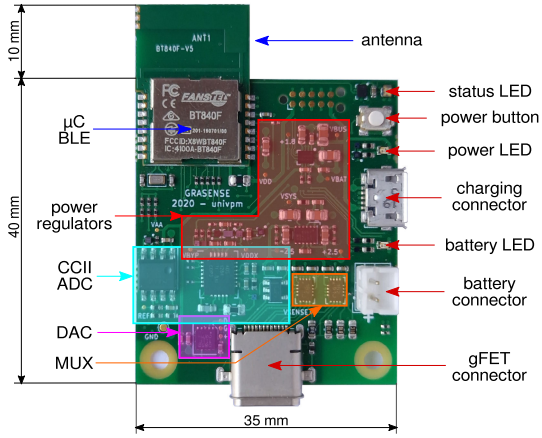

Fig. 2. Picture of the assembled PCB, which measures 35 × 40 mm. The battery can be recharged through the micro-USB connector to the right, while the gFET array is connected to the Type-C USB connector to the bottom. The BLE module on the top left also includes the microcontroller (MCU) that supervises all the system operations.

PCB, excluding the antenna, measures just 35 × 40 mm and is powered by a small (20 × 27.5 × 6 mm) 250-mAh lithium-ion polymer (LiPo) rechargeable battery.

The gFET array is housed in a separate pod (for ease of cleaning and replacement), connected through the bottom Type-C USB connector, chosen for its wide availability, also in waterproof configurations, and large number of available contacts, which allowed us to implement 12 independent drain circuits (perfect for the Graphenea GFET-S20 sensing chips we used in our experiments), a common gate biasing, and auxiliary connections to detect pod attachment and connector orientation.

The required specifications impose strict constraints on the performance, and thus on the component selection, especially of the MOSFET M1 and of the ADC. The transistor must have a gate leakage current (commonly due to ESD protection diodes between the gate and the source) that is negligible with respect to the current being measured. We thus chose for the

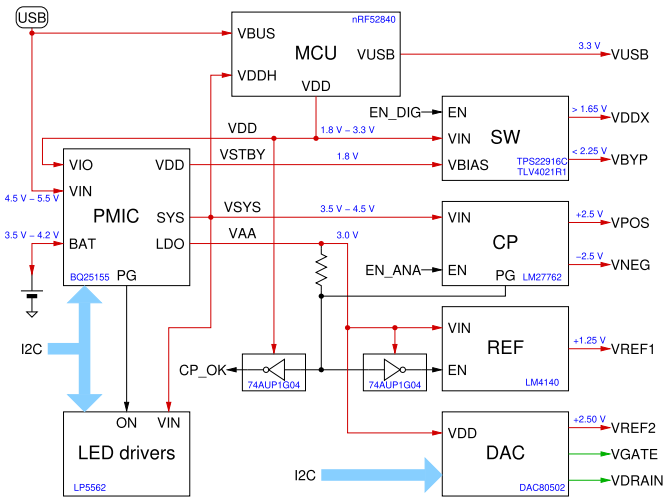

Fig. 3. Block diagram showing the main power and bias voltage generation components of the whole system. Red lines denote the supply voltage rails, with arrows that mark the power flow direction. Some of the digital control and status signals used to ensure proper power sequencing are also reported.

M1 transistor a Texas Instruments CSD13380F3, which has a specified maximum gate-to-source leakage current of 25 nA at $V_{GS} = 8$ V. Operating the transistor at $V_{GS} \simeq V_{TH} = 0.85$ V, because of the voltage-follower op-amp, should result in a much lower leakage.

For the ADC, we chose a Texas Instruments ADS1284 for its very high resolution (31 bits), low noise ($5\,\text{nV}/(\text{Hz})^{1/2}$), and high input impedance (either 1 GΩ or 100 GΩ depending on the operation mode). Unfortunately, it requires a bipolar power supply to operate with input signals near ground. That is nevertheless an unavoidable requirement, because also the other analog components, such as op-amps and MUX, would benefit and offer better linearity near ground if operated with a bipolar supply.

A detailed description of the purpose and operation of all the main circuit subsystems is given in Sections II-A–II-D.

A. Power Management

A block diagram showing the major components of the power subsystem is reported in Fig. 3. The system is battery-powered, so the power management section will have to generate all the required power rails from the rechargeable battery, the ADS1284 being quite demanding in terms of the number of different power rails, requiring five of them. Indeed, it is operated with a +2.5 and −2.5 V bipolar analog supply voltage; in addition, it needs a +1.8 V digital supply VBYP (only when $V_{DD} < 2.25$ V, otherwise it can be generated internally) and the I/O voltage VDDX, which must match the MCU digital supply V_{DD}, and finally a precision +1.25 V reference voltage for the ADC.

The main power management IC (PMIC), which is fully controllable by an I^2C interface from the MCU, handles all the battery charging chores and provides the main system voltage rail VSYS, either from the battery itself (when operating stand-alone) or from the external USB connector input. In the former case, VSYS tracks the battery voltage, and in the latter case it is regulated to 4.5 V. This rail powers the MCU, a

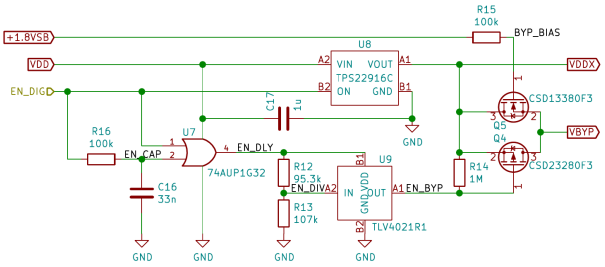

Fig. 4. Schematic of the ADC digital supply sequencing circuit.

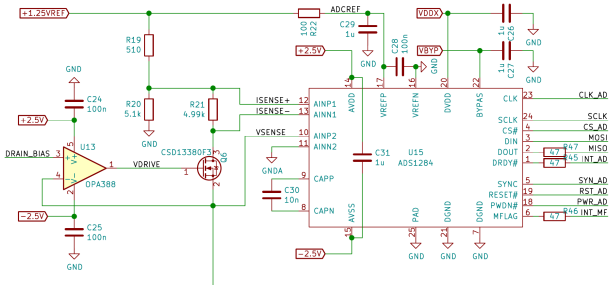

Fig. 5. Schematic of the current conveyor and ADC connections.

Nordic Semiconductor nRF52840 (which has an embedded BLE transceiver), and the low-noise regulated charge pump (CP) for the bipolar supply.

This particular MCU was selected not only because it is one of the lowest power, best performing BLE-enabled MCU, but also, quite importantly for this application, because it is one of the very few that can be directly powered by a LiPo battery, having an integrated dual-stage switching step-down dc/dc converter. Indeed, the main digital rail VDD is derived from its first stage, which is software-programmable between 1.8 and 3.3 V, while the second stage is dedicated to the MCU internals and radio. Compared with external converters, this solution makes it much easier to achieve very low stand-by powers as the converters themselves can be conveniently shut down at light loads under the supervision of the MCU.

The PMIC also has an embedded low-dropout (LDO) regulator which is used to derive a clean and regulated analog supply VAA from VSYS, for the voltage references (REF) and DACs. It also provides a regulated, fixed 1.8 V, low-current rail for stand-by power, typically used to supply real-time clocks (not implemented in the current prototype), since it is also present when the main rail is switched off. This fixed 1.8 V voltage has been used to bias the digital rails switch circuit (SW), which must provide the correct digital power rails to the ADC, as shown in Fig. 4.

The SW circuit is essentially a high-side load switch, with a controlled slew rate to prevent brown-outs on the MCU VDD rail (which would cause system resets when attempting to enable the ADC). Since the value of V_{DD} voltage is under software control (in the 1.8–3.3 V range, with 0.3 V increments) and a fixed value cannot be ensured throughout firmware development, and even initial MCU programming, the switch must ensure that no more than 2.25 V is applied to the ADC. A voltage comparator thus ensures that the VBYP rail gets disconnected in such a case, and we added a turn-off delay to give it time to be fully discharged when the subsystem gets disabled.

B. Current Conveyor and Acquisition Chain

Fig. 5 shows the schematic of the current conveyor, together with how the sensing resistor is connected to the ADC.

The desired sensor biasing voltage (VDRAIN, from the DAC) is applied to the measuring terminal (through the MUX) by means of the voltage-follower built using the op-amp and the MOSFET. The current drawn from the measurement terminal is then sensed from the other side of the MOSFET by a sensing resistor and differentially measured by the ADC first channel. The resistor divider from which the sensing current is obtained is used to lower the maximum common-mode voltage at the ADC input, as it cannot operate near the positive rail.

Moreover, for proper operation, it is essential that the op-amp and ADC input bias currents, as well as the MOSFET gate–source leakage, be negligible or at least accounted for in the measure through individual (automatic) sensor calibration. To aid this, the second ADC channel monitors the sensor biasing voltage actually applied to the MUX (after the voltage follower stage), so that amplifier offsets and the effect of bias currents can be sensed and compensated for.

Indeed, ADS1284 is a very high-resolution (31 bits) ADC which has, by design, quite significant offset ($\pm 50\,\mu$V) and systematic gain (-1%) errors. They can both be internally compensated using two dedicated 24 bit calibration registers: OFC and SFC. They apply offset and gain compensation in the digital domain after the on-chip filters have transformed the sigma–delta ADC bitstream into 32 bit signed digital words, as follows:

$$N_{\mathrm{ADC}} = \left(\frac{V_{\mathrm{in}} + V_{\mathrm{os}}}{V_{\mathrm{REF}}} \cdot A_{\mathrm{V}} \cdot 2^{32} - N_{\mathrm{OFC}} \cdot 2^{8} \right) \cdot \frac{N_{\mathrm{FSC}}}{2^{22}} \quad (1)$$

where N_{ADC} is the output word that is transmitted to the MCU through the SPI interface, N_{OFC} and N_{FSC} are the values of the corresponding calibration registers, V_{in} is the differential input voltage selected from the input MUX, V_{os} is the analog offset of the programmable-gain input amplifier, and A_{V} is the overall analog chain gain, which can be expressed as

$$A_{\mathrm{V}} = k_{\mathrm{PGA}} \cdot \frac{R_{\mathrm{ADC}}}{2\,R_{\mathrm{PGA}} + R_{\mathrm{ADC}}} \cdot \frac{R_{\mathrm{REF}} + R_{22}}{R_{\mathrm{REF}}} \quad (2)$$

where $k_{\mathrm{PGA}} = 2^{n}$, $n \in \{0, \ldots, 6\}$, is the nominal input programmable amplifier gain, $R_{\mathrm{ADC}} = 55\,\mathrm{k\Omega} \cdot (1 \pm 20\%)$ is the differential sigma–delta converter equivalent input resistance, $R_{\mathrm{PGA}} = 300\,\Omega \cdot (1 \pm 10\%)$ is the PGA output resistance, main cause of the systematic gain error, while $R_{\mathrm{REF}} = 85\,\mathrm{k\Omega}$ slightly compensates it due to the external noise filter resistance $R_{22} = 100\,\Omega$, which lowers the actual full-scale reference of the converter, so that A_{V} becomes

$$A_{\mathrm{V}} = k_{\mathrm{PGA}} \cdot 99.0\% \cdot (1 \pm 0.25\%). \quad (3)$$

Note that 0.25% tolerance on A_{V} is greater than the accuracy of the voltage references (0.1%) used for both the ADC and the DAC, so on-line, in-circuit calibration of the gain through FSC using, e.g., the DAC as a reference, is beneficial and can provide more than a twofold increase in accuracy.

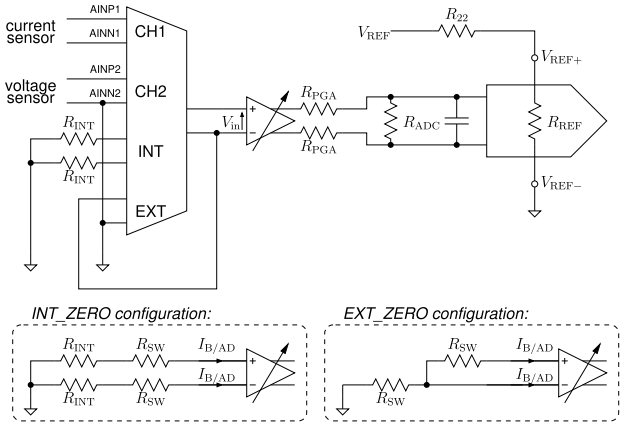

Fig. 6. Simplified input equivalent circuit of the ADC in the used configuration, with details of the input MUX showing internal and parasitics resistances for the internal offset calibration INT_ZERO ("INT" position) and the external offset calibration EXT_ZERO ("EXT" position) modes. R_{SW} are the MUX switch resistances, while R_{REF} is the equivalent resistance of the ADC voltage reference input, which is actually a switched capacitor circuit.

The value to store in the calibration registers can be computed in firmware by following a suitable calibration procedure, which is also able to correct some of the external error sources, as will be detailed in Section II-C.

C. Automatic Calibration

1) Voltage Channel Calibration: The first things that should be calibrated are the internal offset and gain errors of the ADC itself, so that it can be later used to measure and compensate other error sources. This can be done by programming the internal MUX to zero V_{in}. It has two ways to do so, as depicted in Fig. 6: either by connecting both PGA inputs to a common voltage (approximately ground) through $R_{INT} = 400\,\Omega$ resistors or by shorting the PGA inputs through a switch with an ON-resistance $R_{SW} \simeq 30\,\Omega$, and connecting the inverting input to AINN2, which is ground. The first configuration, which we call INT_ZERO, can be used to estimate V_{os}, and the second one, EXT_ZERO, to estimate the bias current $I_{B/AD}$ flowing into the PGA inputs.

Having preliminary set $N_{OFC} = 0$, $N_{FSC} = 2^{22}$, and the input mux to the INT_ZERO configuration, it is thus possible to measure the internal offset V_{os}, since the bias currents (assuming they are matched) only cause common-mode voltage drops across $R_{SW} + R_{INT}$, leading to $V_{in} = 0$ in (1). So, letting $N_{ADC}^{INT\_ZERO} = 2^{32}\,A_V\,V_{os}/V_{REF}$ be the corresponding digital readout, we can pose

$$N_{OFC} = N_{ADC}^{INT\_ZERO}/2^8. \tag{4}$$

On the other hand, setting the input mux to the EXT_ZERO configuration leads to $V_{in} = -R_{SW}\,I_{B/AD}$, so if $N_{ADC}^{EXT\_ZERO}$ is the corresponding digital readout, the bias current can be estimated as

$$I_{B/AD} = \frac{N_{ADC}^{INT\_ZERO} - N_{ADC}^{EXT\_ZERO}}{2^{32}} \cdot \frac{V_{REF}}{A_V\,R_{SW}}. \tag{5}$$

Next, to estimate A_V and hence set the FSC register, we need to apply a differential input voltage as high as possible. This can be done through the DAC, as it has a much lower stated gain error than the ADC. After setting the OFC register to the value computed with (4), the DAC is first set to output a low voltage $V_{LOW} = V_{REF}\,N_{DAC}^{LOW}/2^{16} \simeq 10\,\text{mV}$, (not 0 V to avoid possible nonlinearities operating the DAC near to, or below, its low rail, since its offset, which should be within $\pm 1.5\,\text{mV}$, is not yet determined), and the corresponding N_{ADC}^{LOW} value is acquired from the second ADC channel and recorded. The procedure is repeated for $V_{MID} = V_{REF}\,N_{DAC}^{MID}/2^{16} \simeq 500\,\text{mV}$, which is close to the ADC full-scale range of $\pm V_{REF}/2$, to yield N_{ADC}^{MID}, so that

$$N_{ADC}^{MID} - N_{ADC}^{LOW} = \frac{V_{MID} - V_{LOW}}{V_{REF}} \cdot A_V \cdot 2^{32} \tag{6}$$

since the measure was done with $N_{FSC} = 2^{22}$. Solving for A_V yields

$$A_V = \frac{N_{ADC}^{MID} - N_{ADC}^{LOW}}{N_{DAC}^{MID} - N_{DAC}^{LOW}} \cdot \frac{1}{2^{16}}. \tag{7}$$

The aim of gain calibration is to make A_V close to its ideal value, i.e.,

$$A_V \cdot \frac{N_{FSC}}{2^{22}} = k_{PGA} \tag{8}$$

which yields

$$N_{FSC} = 2^{22+16+n} \cdot \frac{N_{DAC}^{MID} - N_{DAC}^{LOW}}{N_{ADC}^{MID} - N_{ADC}^{LOW}}. \tag{9}$$

The information thus gathered can also be used to correct the offsets of the DAC and the current conveyor op-amp. By denoting with N_{CCO} such combined offset, expressed in DAC units, it results

$$N_{CCO} = \frac{N_{ADC}^{LOW} - N_{ADC}^{INT\_ZERO}}{2^{16} \cdot A_V} - N_{DAC}^{LOW} \tag{10}$$

which can be easily computed using the value of A_V estimated from (7), and then subtracted in firmware from the desired DAC codeword. Of course, such digital compensation can only work up to the resolution of the DAC, which is around $20\,\mu\text{V}$. Of the fractional part, which cannot be compensated in hardware, we will take care during the current channel calibration, as discussed next.

2) Current Channel Calibration: The current is measured by digitizing the voltage drop across a sensing resistor RS (see Fig. 1). So, if the voltage acquisition chain is well calibrated and the value R_S of the sensing resistor is known, the main remaining error sources are the bias and leakage currents at the sensing node (source terminal of M1). Let us denote with V_D the voltage at such node. Ideally, it should be $V_D = V_C - V_o$, with $V_C = V_{REF}\,N_{DAC}/2^{16}$ being the desired voltage and V_o the residual offset mentioned above, hopefully $|V_o| < 10\,\mu\text{V}$. Let us also call I_o the sum of the leakage and bias currents from that node. As a first-order approximation, the leakage can be supposed to be proportional to V_D, while the bias can be assumed constant, so that we can use the following model:

$$I_o = I_B + V_D/R_L. \tag{11}$$

It is actually possible to measure I_o in-system, by sweeping V_D and keeping the MUX disabled. Linear regression allows easy identification of I_B (e.g., $-1.6\,\mu A$ on a sample prototype) and the leakage resistance R_L (e.g., $998.3\,k\Omega$ on the same prototype, mainly due to the $1\,M\Omega$ bias resistor to ground). It is theoretically possible to correct the fit for V_o but, given the magnitude of R_L, the correction would be totally negligible.

In practice, it is better to measure $V_{A\,off} = R_S\,I_o$ every time V_D is changed, by temporarily disabling the MUX, and then subtract its value from the ones measured on the active channels. That way, not only are the leakage currents compensated but also the residual offset of the ADC will be.

By connecting a precise calibration resistance R_{CAL} to one active MUX channel, the voltage V_A across the sensing resistor will thus be read as

$$V_A = R_S\left(\frac{V_D}{R_X} + I_o\right) - V_{A\,off} = \frac{R_S}{R_X}\,V_D \tag{12}$$

where $R_X = R_{MUX} + R_{CAL}$ is the series of the ON-state MUX resistance, to be determined, and the selected known calibration resistance.

A simple and robust way to simultaneously estimate R_{MUX} (which is a very small resistance, few ohms nominally), R_S (so that its tolerance does not add up to that of the calibration resistors), and V_o is to measure the I–V relationship for two different values of R_{CAL}; let us call them $R_{CAL\,1}$ and $R_{CAL\,2}$ and perform a linear regression to average out DAC and ADC nonlinearities. The result would be the coefficients k_i and $V_{B\,i}$ for the two regression lines

$$\begin{cases} V_A = k_1\,V_C + V_{B\,1}, & \text{with } R_{CAL} = R_{CAL\,1} \\ V_A = k_2\,V_C + V_{B\,2}, & \text{with } R_{CAL} = R_{CAL\,2} \end{cases} \tag{13}$$

an example of which can be seen in Fig. 7. From (12), it can be seen that the intersection of the two regression lines can only happen at $V_A = 0$ and $V_D = 0$ (the only solution for two *different* resistances that carry the same current when subject to the same voltage is the null solution).

Due to measurement noise, the compensation of $V_{A\,off}$ cannot be exact so V_A at intersection, $V_{A\,int}$, will not be exactly zero, but as shown in Fig. 7 it is still very small, while V_C at intersection, $V_{C\,int}$, equals V_o. From (13)

$$V_o = V_{C\,int} = \frac{V_{B\,2} - V_{B\,1}}{k_1 - k_2} \tag{14}$$

$$V_{A\,int} = k_1\,V_o + V_{B\,1} = k_2\,V_o + V_{B\,2}. \tag{15}$$

Imposing $V_{A\,int}$ to be exactly zero is theoretically possible, but that would make the parameter fitting problem nonlinear, with repercussions on the computational complexity of the MCU firmware but negligible effects on the estimated parameters, as verified with MATLAB simulations.

Finally, being $k_i = R_S/(R_{MUX} + R_{CAL\,i})$, it is possible to estimate the sensing and parasitic resistances

$$R_S = \frac{k_1\,k_2}{k_1 - k_2}\,(R_{CAL\,2} - R_{CAL\,1}) \tag{16}$$

$$R_{MUX} = \frac{k_2\,R_{CAL\,1} - k_1\,R_{CAL\,2}}{k_1 - k_2} \tag{17}$$

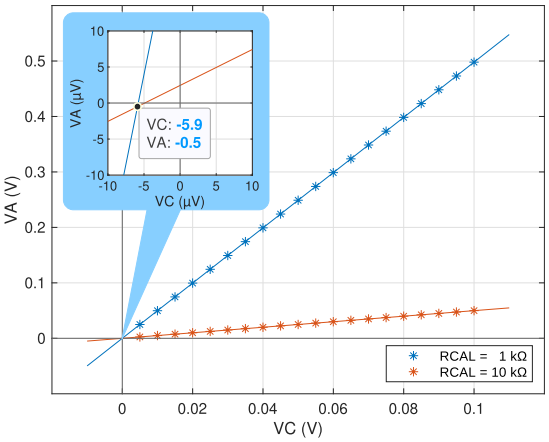

Fig. 7. Estimation of residual DAC and ADC offsets. Stars denote measurement points for two different calibration resistors, and the solid lines are their linear regression. The intersection between the regressors represents the sought offsets, as highlighted in the inset, which shows the intersection at $V_C = -5.9\,\mu V$ and $V_A = -0.5\,\mu V$.

so that the best estimate of the current I_A is

$$I_A = \frac{V_A - V_{A\,int}}{R_S} \tag{18}$$

so that the resistance R attached to the MUX is

$$R = \frac{V_C - V_{C\,int}}{V_A - V_{A\,int}}R_S - R_{MUX}. \tag{19}$$

3) Gate Drive Calibration: The gate drive DAC shares the same reference as the drain voltage-setting DAC, but aside from that it is an independent unit and so its offset should be independently calibrated. This is a relatively easy task to do after the rest of the system is calibrated. By connecting a protection resistor (its precise value is not important, we used $3.9\,k\Omega$) between the gate drive and a MUX channel, it is theoretically possible to sweep the calibrated "drain" voltage until the current across the protection resistor is zero. This way the "exact" gate drive voltage can be determined and its offset derived and compensated for in firmware. In practice, since the CCII we implemented does not allow backward currents through, the "drain" sweep on V_D can only be performed for voltages higher than the "gate" drive V_G. Linear regression, fitting the measured points V_D, I_A to the line $I_A = g_x\,(V_D - V_G)$, still allows the accurate determination of the offset voltage on V_G (and of the conductance g_x of the connected protection resistor).

D. Sensor Pod Attachment and Monitor

The acquisition device is connected to the sensor pod via a Type-C USB connector with the pinout customized as shown in the top of Fig. 8. Care has been taken to ensure that no damage is done if erroneously connected to a standard USB port, as only the data lines have been used to carry signals.

Moreover, the VBUS, CC1, and CC2 lines are all monitored via suitable resistor dividers connected to the MCU internal ADC channels, to detect the attachment (and orientation, being the connector reversible) of the pod. The pod, indeed, has the P:1 line shorted to ground, while the P:2 line is open, so it allows easy identification of the connector orientation.

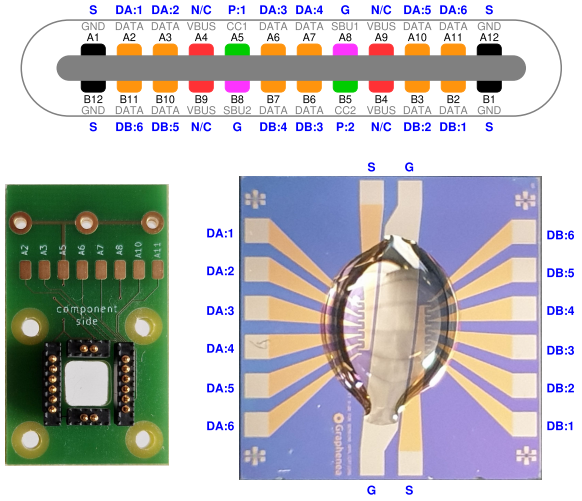

Fig. 8. Sensor pod interface pinout (top): the 24-pin Type-C USB connector has four ultrahigh-speed data pin pairs (at the sides) and two high-speed pin pairs (in the middle); those "data" lines have instead been used to connect the 12 drain terminals DA:1–6 and DB:1–6 of the Graphenea GFET-S20 chip (pictured at the bottom right, magnified 4×, with a drop of saline solution on top of the active areas for liquid-gating). The sources (S) are at ground, while the gates (G) are connected through the SBU pins. The prototype pod (bottom left, pictured in scale 1:1) uses spring-loaded pins that match the pads on the GFET-S20 chip and connects the presence-detect pin P:1 to ground, leaving P:2 open, to allow orientation detection and thus proper numbering of the drains in the UI software. A custom case automates the alignment of the pins to the chip pads.

Standard USB devices have ∼5 kΩ pull-downs on those lines, while host ports or chargers have pull-ups, thus allowing the firmware to recognize that the proper pod is attached through the CC lines before starting operations, and alerting the user if an improper attachment was mistakenly connected.

The pod then contacts the graphene sensor chip (both visible in the bottom parts of the same Fig. 8) by means of spring-loaded pogo pins, the correct alignment of which is ensured by a custom case and chip holder. This split configuration allows the pod to be easily customized to other sensing chip designs, plus, being so simple and inexpensive, can be conveniently cleaned and/or replaced in case it gets contaminated by the biological agents being tested.

It exposes 12 drain circuits, enough to measure both banks of six gFETs that are present on a GFET-S20 chip. This redundancy is indeed very useful, especially for conducting research with this device, because gFETs are not 100% reliable and every chip may contain a few nonworking devices. Their I–V characteristics will show clearly erratic behavior (they might, e.g., show up as open, shorted, with gate leakage, or just very low gain) and can easily be identified in software and removed from further processing, as will be demonstrated in Section V-C3.

III. Data Transmission

Besides the hardware design, a lot of attention was also devoted to the development of a suitable communication strategy over BLE, with the aims of making the system easy to use, power-efficient, and fast to respond. This led us to chose BLE connection parameters with very short connection intervals (7.5 ms) to ensure fast throughput, but quite high connection latencies (up to ×32 connection intervals) to save power, since most of the communication is from sensor to PC and not the other way around. Moreover, the portable device is designed so that its operation can be completely controlled remotely from the host PC, but it can also perform measurements in complete autonomy, storing the results and sending them to the host PC when connected.

TABLE I
Custom Bluetooth Service "System"

Service UUID: 57491600-59d0-5fbc-bf12-a00ce91bd936

UUID	Length	Props.	Characteristic name & description
1	4	R N	**System state:** HW self-diagnosis result power controllers status battery charger status
2	8	R N	**Radio state:** BLE connection parameters timing information RF signal strength
3	20 12 1 – 8	W N (N) (N) (W)	**Telemetry data:** power supply monitor pod attachment detection system commands: – RTC settings – visual identification (LEDs) – reset and power-off control – firmware upgrade

To this end, two custom Bluetooth services have been designed and implemented in the MCU firmware, besides the mandatory ones and the standard "Device Information" and "Battery Service" services. The custom service UUIDs, for easier referencing in the software and firmware, are derived by prepending to the base X.509 distinguished name "CN = Grasense, OU = DII, O = UnivPM, L = Ancona, C = IT" the service name itself, as shown in Tables I and II, where details of the implemented characteristics are also reported.

The first custom service is "system," which is used to transfer telemetry data (such as power supply status and monitors, system self diagnosis, real-time clock settings, Bluetooth connection information), as depicted in Table I. It has three characteristics, mainly used to receive notifications about the system power, radio, and pod status. The complete UUID of those is obtained by replacing the last nibble of the fourth byte of the service UUID with the number shown in the first column of the table. This is a slow-throughput service, with the order of a new notification per second.

The second custom service is the "measure" service, which is used to configure measurement details such as voltage sweep type and range, speed, active channels, and ADC and DAC calibration. It is detailed in Table II. It has five characteristics, and the measurement results are transmitted to the PC by a stream of notifications on the first one. To achieve maximum throughput, the maximum number of packets as allowed by the BLE stack is squeezed into each connection interval. A complete set of measures (12 sweeps, 256 points per sweep, 32 bits per sample) occupy 12 KiB and can be transferred in a fraction of a second.

TABLE II
CUSTOM BLUETOOTH SERVICE "MEASURE"

Service UUID: 05d52df9-e5c1-5499-aabd-28f7f43374a5

UUID	Length	Props.	Characteristic name & description
1		W N	**Measure data stream:**
	1 – 2	(W)	data streaming control
	1 – 20	(N)	data channel
2	0 – 19	R W	**Measure name:** UTF-8 encoded, human readable
3	10	R W N	**Sweep configuration:** active channels, DAC settings, sweep mode and steps, pod detection
4	2	R W N	**Status register:** measure progress, measure ready
5	32	R W	**Calibration register:** time & temperature of last cal., calibration offsets & gain, calibration resistances, residual errors

The other characteristics are used to set, and eventually retrieve, the measure parameters, and a user-configurable name to ease data cataloging. The system also has a real-time clock that is automatically synchronized to the PC clock by the software, and it is used to automatically timestamp measures.

In particular, the "measure" service was devised so that all the configuration and state data are stored on the device. Because of this, the host PC does not need to stay connected to the device during the measure, and hence the radio can be turned off to reduce electrical noise. All the data and settings are then automatically synchronized again when the Bluetooth connection is reestablished.

IV. USER INTERFACE

All the details of the communication are taken care of by a UI software that we wrote to accompany the acquisition device. A few screenshots of the main panels of the UI are shown in Fig. 9.

The first panel allows the discovery and display of all the nearby active (advertising) sensors. It is also possible to associate a persistent user-definable name to each device for easier identification in case a single PC is used to command and control several acquisition devices simultaneously. From the same panel, it is then possible to establish the BLE connection to the selected device.

The second panel is the main one, where measurement details, such as which channels to activate, sweep parameters (maximum voltages, number of steps), and sampling time, can be set. Measures can be started, either single-shot, or continuously repeated, while the current/voltage or resistance/voltage characteristics are shown in the upper portion and automatically timestamped and saved. It is also possible to request the device to perform the self-calibration procedure from this panel.

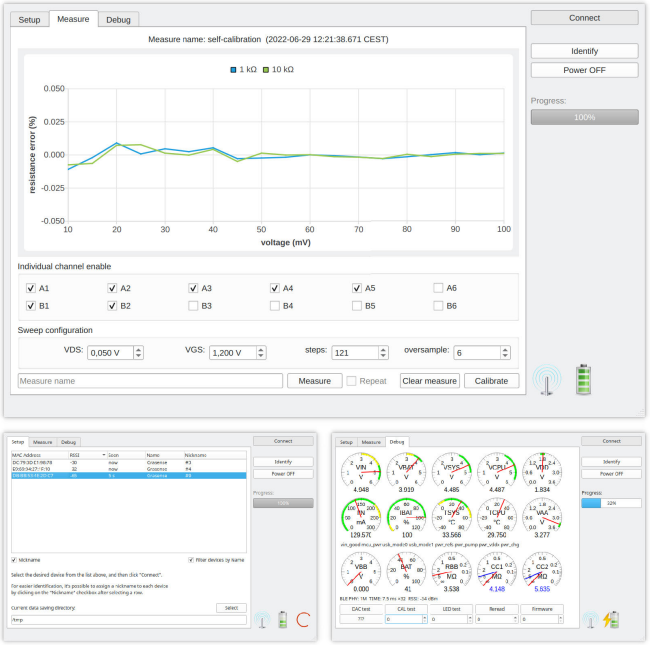

Fig. 9. Example screenshots from the UI. Clockwise from bottom left: 1) the setup panel, where the available devices are listed and the BLE connection to one of them can be established; 2) the measure panel, where the sweep parameters can be configured and the measure results are plotted (showing the self-calibration results in this case); and 3) the debug panel, showing system telemetry and allowing troubleshooting and maintenance tasks (such as OTA firmware upgrades).

Finally, a third panel contains debug information, where basically all the telemetry data received are graphically displayed so that during development it was possible to keep everything under control with a quick glance. It also allows to start over-the-air (OTA) firmware upgrades. The most important parameters for the end user, such as battery level, radio signal strength, and BLE connection status, are also pictorially represented in the bottom right corner of every page.

V. EXPERIMENTAL RESULTS

Several prototypes of the system have been fabricated and used to conduct some tests. In the following, we will first start by presenting some experimental results aimed at validating the operation and performance, including power consumption, of the proposed system. Then, a practical application example to a COVID-19 virus detector will be discussed.

A. Calibration

As previously described, the system includes an in-firmware self-calibration procedure to compensate most offsets and systematic gain errors. The results are stored internally but can also be transferred over Bluetooth for long-term archival, and a sample calibration report is shown in Fig. 10.

As the trims are internally applied, the only information of interest to the user is that highlighted in blue. If the ultimate accuracy is sought, readings can be compensated for those residual offsets, and the estimated value of R_S should be used instead of the nominal 4.99 kΩ. This is indeed already

```
### Grasense self-calibration results file ###
#
#     Device Address : DB:BB:53:4E:2D:C7
#        Device Name : Grasense (#9)
#  Manufacturer Name : DII@UnivPM
#      Serial Number : 0009
#  Hardware Revision : 1.0
#  Firmware Revision : 2022-04-11T19:06:21+02:00
#
#   Calibration Data : 2022-06-24 17:31:21.249 CEST (+27.0 °C)
#
#         DAC offset :  -6.3935 µV  (-21968)
#         ADC offset :  -0.1080 µV  (-371)
#     SMU resistance : 4.989130 kΩ
#     MUX resistance :    2.036  Ω
#
# ADC bias current   :   +10.09 nA  (+1040)
# ADC zero error     :   0.0582 µV  (~200)
# ADC zero trim      : -37.1039 µV  (-498)
# ADC gain trim      : +0.69628 %   (+29204)
# DAC external trim  :    -0.08 mV  (-4)
# DAC internal trim  :    -0.71 mV  (-37)
# DAC residual trim  :  -5.9596 µV  (-20477)
#     midpoint error :   5.6624 µV  (~19456)
#
```

Fig. 10. Example calibration report. The first section identifies the device (the name is user-definable). The second section (highlighted in blue) includes the time and environmental conditions when the calibration was performed, followed by the main parameters that affect the interpretation of the measures: residual offsets, sensing resistance, and parasitic switch resistance. The last section includes additional information detailing the amount of internal trimming applied and the residual errors. Values are reported both in physical units and, when available, in digital units. The main parameters (those highlighted in blue) are also included with every measure performed after calibration.

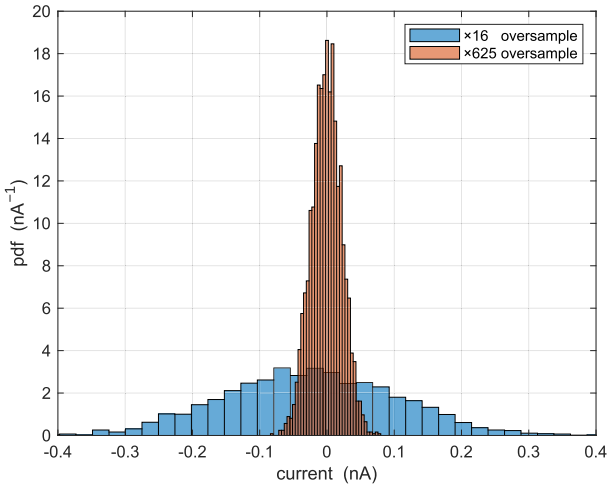

Fig. 11. Distribution of measurement noise for different oversampling factors. A dummy 250-point sweep was performed over all the 12 channels, to obtain a total of 3000 samples, with either a ×16 oversample factor (4.096 ms sampling time) or a ×625 oversample factor (160 ms sampling time), with the measuring pod disconnected. Voltage was fixed at 50 mV. The standard deviation of the distributions (which corresponds to the rms value of the signals) is 130 and 22 pA, respectively.

automatically done by the UI software as these data are included in every measure.

Once the calibration is performed, the remaining errors are mainly due to the (in)accuracy of the references used, being the converters' nonlinearity negligible in their respect. In practice, 0.1% accuracy is expected in current measurements (limited by the embedded voltage reference accuracy), while resistance measurements should be much more precise as the gain errors cancel out, so that a 0.01% (plus 0.1 Ω for MUX channel mismatch) accuracy in resistance measurements can be expected, being limited by the tolerances of the reference resistors.

To validate the effectiveness of the calibration, two tests have been performed. As a first experiment, suitable to evaluate both noise and offset, an open-circuit measure was performed. In all, 3000 samples were obtained using both a standard sampling time of 4.096 ms (×16 oversample), and a long sampling time of 160 ms (×625 oversample), the latter chosen because it is an integral multiple of the mains frequency. A statistical analysis of the results is shown in Fig. 11. As can be seen, offsets are almost perfectly compensated, and the rms values of the remaining noise are 130 and 22 pA, for the short and long sample times, respectively. Being the full-scale range of 100 µA yields a maximum effective resolution of 22 bits, which is reduced by a couple of bits using the standard sampling time.

The second experiment involved measuring a precision (0.01% nominal tolerance) 100 Ω reference resistor. The voltage was swept from 1 to 10 mV and the measure repeated 100 times to verify stability and repeatability, as the test lasted about 80 min. This is quite a stressful test for the device as such a low resistance falls way below the typical value of a gFET device (tens of kilohms), for which the full-scale range

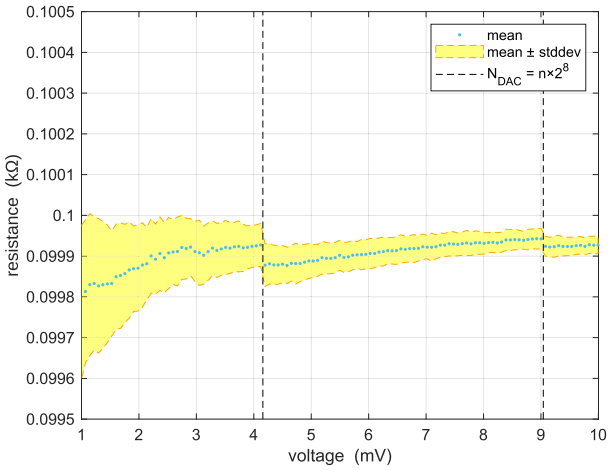

Fig. 12. Results of measuring a 100-Ω reference with an applied voltage swept between 1 and 10 mV in 76.294-µV steps (corresponding to four DAC codeword units). Vertical dashed lines denote the location of codewords 256 and 512, taking into consideration the 0.71-mV (37 units) DAC trim applied in firmware and returned in the calibration report.

was designed. The results are reported in Fig. 12, where the mean and standard deviation of the measures are reported.

As can be expected, tolerances are higher at lower voltages due to the lower currents involved in the measure. Indeed, the standard deviation σ_R is almost exactly inversely proportional to the applied voltage, resulting in $\sigma_R V_D/R \simeq V_{noise} = 2.13\,\mu V \cdot (1 \pm 5\%)$ for this $R = 100\,\Omega$ resistor. The same formula can be used to estimate the goodness of fit for the 1- and 10-kΩ calibration resistors (an example of which is shown in Fig. 9), which resulted in $V_{noise} = 1.17\,\mu V \cdot (1 \pm 5\%)$.

The DAC differential nonlinearity (DNL) is also apparent as there are discernible steps when the DAC codeword crosses multiples of 2^8 (whose positions are highlighted by vertical dashed lines). The residual 0.1 Ω offset with respect to the nominal value is probably due to mismatches of R_{MUX}

TABLE III
DEVICE CURRENT CONSUMPTION

#	mode	current*	time⋆	notes
0	OFF	10 nA	∞	1
1	STAND-BY	0.32 mA	20 min	1
2	SLOW ADVERTISING	0.79 mA	10 min	
3	FAST ADVERTISING	1.83 mA	30 s	
4	CONNECTED (IDLE)	2.75 mA	∞	2
5	TRANSMITTING	7.22 mA	0.5 s	2,3
6	MEASURING	16.8 mA	29.5 s	3

∗: currents measured at 3.7 V battery voltage, 20 °C ambient temperature.
⋆: ∞ means not limited in firmware.
1: exiting these modes requires user intervention (pressing power button)
2: BLE connection parameters: 2M PHY 7.5 ms × 32.
3: for 12 channels, 121-point sweep, 16× oversample.

TABLE IV
ENERGY CONSUMPTION BREAKDOWN

subsystem	current	energy⋆	contribution
MCU (idle) + PMIC	26.7 µA	2.96 mJ	0.16 %
LED	2675.3 µA	296.96 mJ	16.09 %
LDO	15.2 µA	1.66 mJ	0.09 %
CP + OPA + REF	4864.8 µA	531.00 mJ	28.76 %
DAC	1358.7 µA	148.30 mJ	8.03 %
ADC	7684.8 µA	838.79 mJ	45.43 %
MCU (measuring)	168.0 µA	18.34 mJ	0.99 %
MCU (transmitting)	4518.5 µA	8.36 mJ	0.45 %

⋆: energy consumption computed considering a 30 s total duration:
"idle" MCU current, PMIC, LED, for all of the 30 s;
"measuring" MCU current, LDO, CP+OPA+REF, DAC, ADC, for 29.5 s;
"transmitting" MCU current for 0.5 s.

between channels, as obviously this reference resistor was connected on a different channel than the ones used for calibration, and is totally within specifications.

B. Power Consumption

Power consumption is a key parameter for portable devices, and we thus carefully tested the amount of power drawn by the acquisition device under its different operating modes. A summary of the results is shown in Table III, which reports the total current absorbed by the device in each of its seven major operating states (or "mode," as described below) together with the time the device can spend, or typically spends, in each of those.

In the OFF mode (state #0), all the power rails are disabled, and the PMIC has a specified leakage current of just 10 nA, much lower than a typical battery self-discharge rate (even a very conservative self-discharge of 0.1% per month would be equivalent to a 350 nA leakage).

When the system is turned on, it starts in the FAST ADVERTISING mode (state #3), with a 152.5 ms advertising interval, to allow quick Bluetooth connection. Then it either goes to state #4, when a BLE connection is established, or spontaneously transitions to the progressively lower power modes (states #2, #1, #0) after a timeout as specified in the "time" column. If, e.g., no connection is established within the first 30 s, the advertising interval is increased to 1.285 s to save power, and halted altogether after 10 min. Actually, the power consumption in states #1–#4 is essentially due to the indicator LEDs, as the MCU and radio draw less than 0.1 mA in these states, and all the other subsystems are powered off. But we preferred to give the operator a clear and immediate visual indication of the device state.

Of course, the power consumption increases significantly when the device is actually performing measures (state #6). Indeed, activation of the analog chain also requires that the +2.5, −2.5, and +3.0 V rails are energized and the A/D and D/A converters enabled, bringing the current consumption up to about 17 mA. Transmitting the data (state #5) then requires lot of radio activity, resulting in about 7 mA of current for an output power of 0 dBm. Since it only takes half a minute to measure 12 channels, and half a second to transmit the measured data back to the PC, the device can still perform well over a thousand measures on a single battery charge. Considering it takes several minutes to prepare the biological sensing element, it can be (and has been) used for weeks of continuous on-field work.

To better understand how the different subsystems contribute to the power consumption, a breakdown of the current drawn by each is presented in Table IV. The breakdown was obtained by selectively powering and enabling individual subsystems in firmware using the control signals depicted in Fig. 3. Though the granularity with which individual parts can be enabled is not at the IC level, it is still possible to single out the contributions of the MCU, which also integrates the BLE radio, from a few other subsystems like the LED driver, the LDO used to power the +3.0 V rail, the analog chain (including the CP that powers the +2.5 and −2.5 V rails), and the converters. Of course, the current drawn by the MCU strongly depends on the code its CPU runs, so we further broke it down between idle consumption and the current drawn while driving the ADC converter and while transmitting the measure results over BLE. Besides the measured current, the table also reports an estimation of the energy consumed, obtained by multiplying the current by the battery voltage and by the time each subsystem stays active (as reported in the notes beneath Table IV). The individual contribution of each subsystem to the total energy expenditure, considering a complete measurement cycle lasting 30 s in total, is also reported in the last column. As can be seen, the majority of the power is destined to the analog chain, with the CP, current conveyor, and ADC drawing three-fourth of the total power, while the MCU and BLE transmission only contribute with a negligible draw of 0.99% and 0.45%, respectively. Overall, a measure requires 1846 mJ of energy (the battery stores more than 3 kJ of energy), with a peak power of 62 mW. For comparison, the system [28], which uses the same gFET devices, consumes 60 mA from a ±9 V supply, leading to over 1 W of power consumption.

C. Transistor Characterization

1) Silicon MOSFET Characteristics Comparison: This acquisition system was specifically designed to accurately capture the I–V characteristics of gFETs, so its voltage and current ranges are tuned to maximize resolution for this use case, which involves low currents (<100 µA for typical gFET sensors) at low drain voltages (<100 mV to avoid electrochemical reactions in liquid-gating).

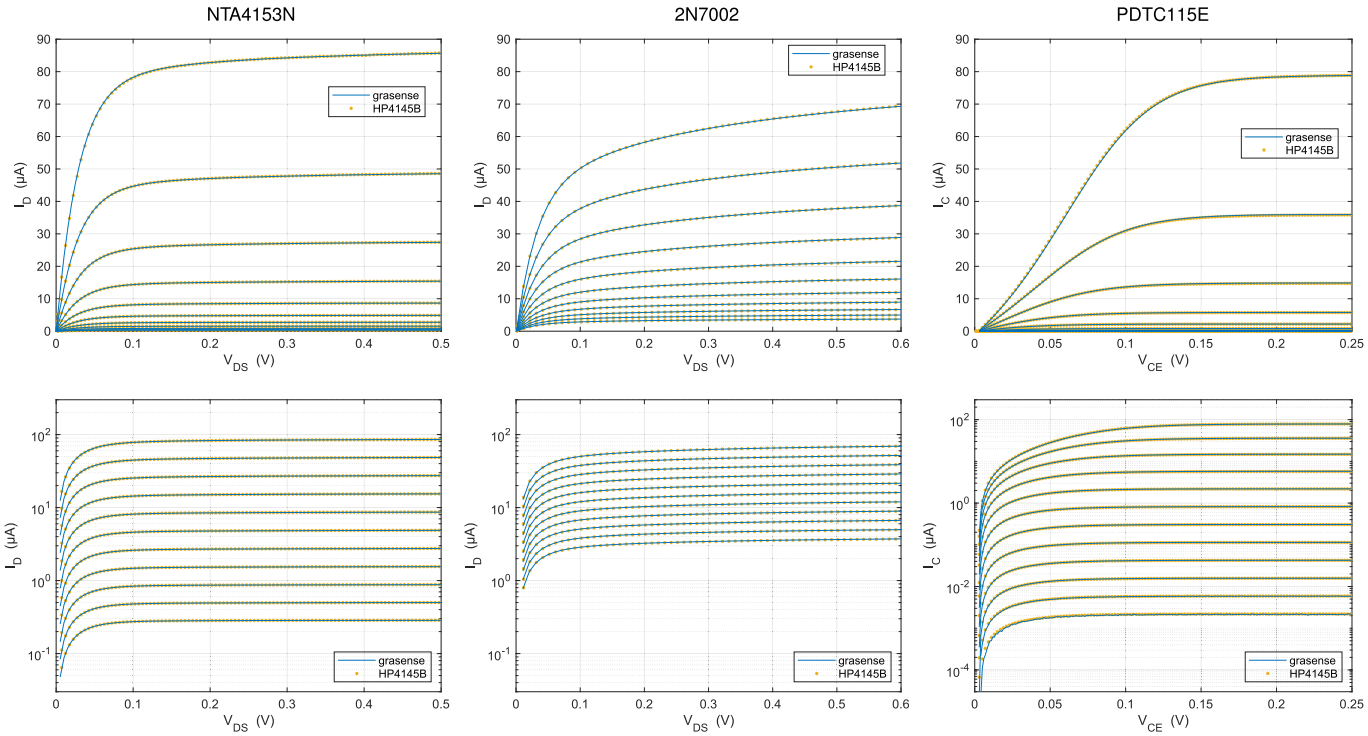

Fig. 13. Output characteristics of various silicon transistors measured both with the presented acquisition device (grasense) and with a semiconductor parameter analyzer laboratory instrument (HP4145B). Top: linear scale to show the typical output response. Bottom: logarithmic scale to better highlight the submicroampere accuracy and the uniform increments due to the exponential gain (for the MOSFET in the subthreshold region and the BJT at low base currents). From left to right. 1) An On Semiconductor NTA4153N power MOSFET in the subthreshold region, measured for gate voltages ranging from 500 to 750 mV in 25-mV increments. Instrument offsets have been adjusted by +2.27 mV (drain voltage) and –0.99 mV (gate voltage) to ensure the I_D curves cross the graph origin and to normalize the vertical axis. 2) An On Semiconductor 2N7002 signal MOSFET, measured for gate voltages ranging from 1.800 to 2.050 V in 25-mV increments. Instrument offsets have been adjusted by +1.64 mV (drain voltage) and +2.07 mV (gate voltage). This device was connected to a different SMU of the HP4145B than the previous one, hence the different offset compensations. 3) A Nexperia PDTC115E BJT, measured for external base voltages ranging from 0.600 to 1.150 V in 50-mV increments. Instrument gain has been adjusted by +2.00% (roughly equivalent to –1 mV offset adjustment of the base drive) to normalize the vertical axis.

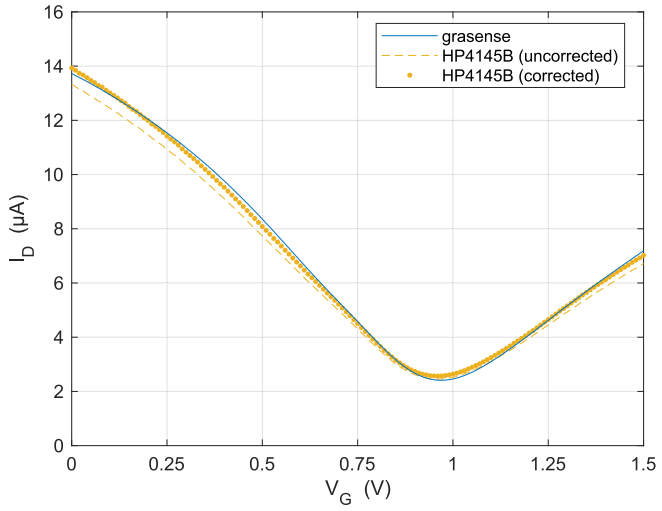

Fig. 14. Measured transfer characteristic of a single Graphenea GFET-S20 transistor, both with the presented acquisition device (grasense) and with a semiconductor parameter analyzer laboratory instrument (HP4145B), using liquid-gating with a simple phosphate-buffered saline (PBS) solution, with a fixed drain–source voltage of 50 mV. The HP4145B data were corrected for 4.54% gain error which results from the +2.27 mV offset of this SMU, which is the same one used for the NTA4153N drain current shown in Fig. 13.

Still, the system is also capable of measuring traditional FETs as it can apply up to +500 mV of drain voltage (at full current, or up to +1 V at reduced currents) and up to +2.5 V of gate drive. So, for the first experiment, we measured a standard On Semiconductor NTA4153N transistor and compared the results with those obtained by a rack-mounted laboratory instrument, an HP4145B semiconductor parameter analyzer. A silicon-based FET was chosen for this comparison because it is inherently more stable than a liquid-gated transistor, so its characteristics are more likely to remain the same in the few seconds that are necessary to reconnect the pod from an instrument to the other. A comparison of the obtained characteristics, after compensating for the HP4145B offsets (which should be within ±10 mV nominal), is shown in Fig. 13 (left).

The NTA4153N is a power MOSFET, so to keep the currents within the acquisition device compliance, we operated it in the subthreshold region. This region also turns out to be really suitable for this type of comparison as it manifests an exponential dependence of the drain current on the gate voltage, so small offsets due to different gate contact materials, cabling, connectors, etc., or slight miscalibration of the instruments, after aligning the horizontal axis (adjustment of the V_{DS} offset) only lead to a multiplicative factor in the drain current, which is also easily estimated and accounted for. Indeed, the subthreshold current for this particular transistor increases by 198 dB/V with the gate voltage, so what appears

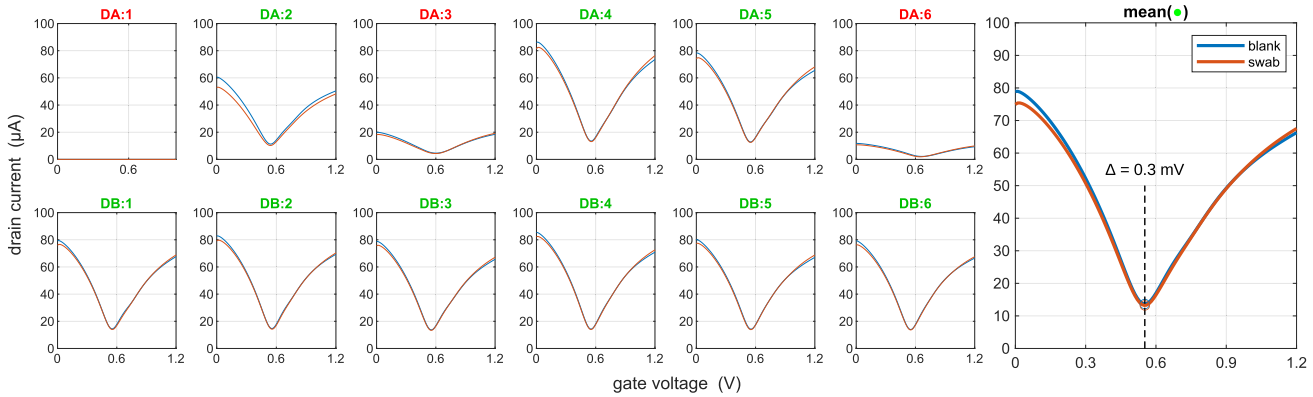

Fig. 15. *I–V* characteristics of a Graphenea GFET-S20 functionalized as described in [25] before (blue line, "blank") and after (red line, "swab") adding to the liquid-gating samples of a nasopharyngeal swab taken from a patient negative to COVID-19, for $V_{DS} = 50$ mV.

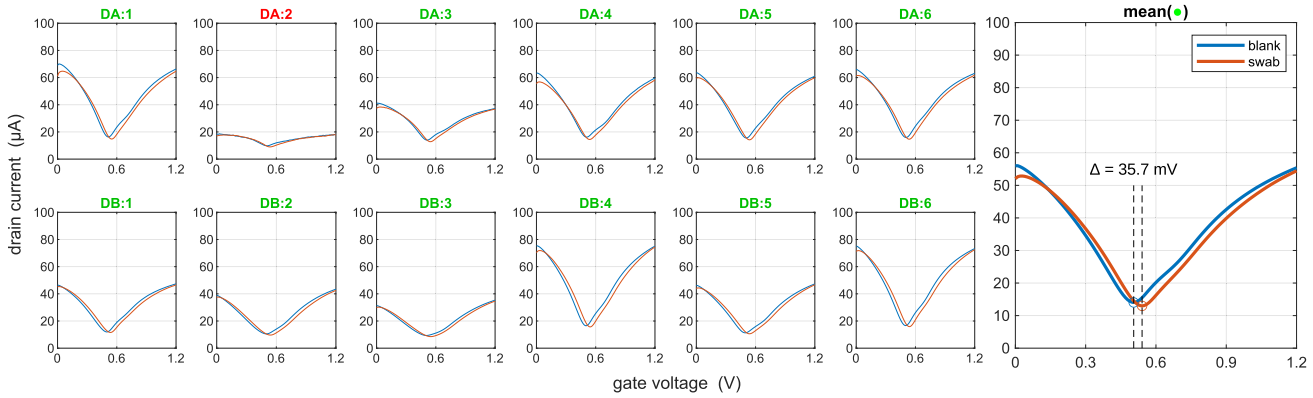

Fig. 16. *I–V* characteristics of a Graphenea GFET-S20 functionalized as described in [25] before (blue line, "blank") and after (red line, "swab") adding to the liquid-gating samples of a nasopharyngeal swab taken from a patient positive to the BA.2 variant of COVID-19, for $V_{DS} = 50$ mV.

to be a 2.27% gain error can actually be explained by a 0.99 mV offset in the gate drive.

To further prove the system accuracy, a higher threshold, logic-level switching MOSFET, an On Semiconductor 2N7002, was also tested. Due to its lower gain, we could operate it much nearer to its threshold, without exceeding our SMU compliance. The results of the comparison, after offset adjustment as per the previous test, are reported in the same Fig. 13 (middle).

2) Silicon BJT Characteristics Comparison: The system can also be used to measure the output characteristics of bipolar junction transistors, and an example for a Nexperia PDTC115E prebiased n-p-n BJT is reported in Fig. 13 (right). The transistor incorporates a 100 kΩ/100 kΩ resistor divider (biasing network) at the base terminal, which basically just halves the applied base voltage at the current levels tested, especially the lower ones. As can be seen, there is excellent agreement in the measured characteristics over more than five orders of magnitude of collector currents, from fractions of nanoamperes to hundreds of microamperes.

3) gFET Characteristics Acquisition: Liquid-gated devices present inherently less repeatability, so accurate comparison between a laboratory instrument and our system is not simple. Nevertheless, we tried to measure a single Graphenea GFET-S20 transistor by attaching it to the same SMU of the HP4145B whose offsets were already determined. The results, shown in Fig. 14, highlight a very good match, considering that the transistor was moved between instruments and so liquid-gating was somewhat perturbed by the mechanical stress of pod reattachment.

Finally, after having validated the performance of the acquisition system, it was tested on its primary usage target, gFETs, using Graphenea GFET-S20 sensing devices functionalized with an engineered dimeric ACE2 receptor, as a proof-of-concept system for a novel type of virus detector [25]. A relatively large-scale clinical trial was conducted using the proposed device. A total of 420 measurements were analyzed, including 180 from nasopharyngeal swabs collected from 25 different subjects. Of these, 75% tested positive for several SARS-CoV-2 variants. The device showed high sensitivity, achieving one of the lowest limits of detection (LODs) compared with other graphene-based sensors. Specifically, it was capable of detecting as little as 65 virus copies/mL without the need for any preprocessing steps.

A sample of the obtained $I–V$ characteristics is shown in Figs. 15 and 16. In the figures, individual $I–V$ curves from the single gFETs are shown, having performed the measurement on a blank chip (functionalized with the receptors but without adding a sample of the potentially virus-carrying agent), and after adding the sample to be analyzed. As can be seen, a few gFETs, marked in red, manifested erratic behavior and had been thus excluded. All the remaining, marked in green, have been averaged and the resulting curves are reported in the bigger panel at the rightmost end. The quantity of interest is

usually the shift in the Dirac point (minimum of the curves), which can be quite tiny, hence the high accuracy requirement.

In particular, Fig. 15 shows the case where the added agent did not contain the target virus, and so the displacement of the Dirac point was negligible, 0.3 mV. Fig. 16, on the other hand, reports the case where the added sample actually contained the target virus, and the shift was a hundred times bigger, 35.7 mV.

VI. Conclusion

This article presented a high-accuracy, self-calibrating, portable acquisition system specifically developed to accurately measure I–V characteristics of gFET-based biological sensors.

Due to the delicate nature of the sensing elements, especially while doing scientific research to develop the desired functionalization of the sensing surface, the system was designed to accurately measure very low currents at low driving voltages, so as not to alter the electrochemical properties of the gating solution.

Indeed, it has nominal current measurement accuracy of 0.1%, limited by the accuracy of the embedded references, up to a maximum of 125 μA, and we measured an rms noise value as low as 22 pA (yielding 22 bits of effective resolution). If need be, different current ranges can easily be accommodated for by changing the sensing resistor, whose value does not even need to be known in advance as it is automatically determined. It can also measure resistances (channel resistances) with a nominal accuracy of 0.01% ± 0.1 Ω, limited by the DAC DNL and the MUX ON-resistance mismatch, in the range from 100 Ω to 1 MΩ, and with a measured rms noise as low as 2.13 μV.

Its compact dimensions, remote controllability through any Bluetooth-enabled PC, and a long battery life of several weeks of typical continuous usage are all characteristics that make it suitable for on-field operation even in the presence of biologically hazardous agents such as pathogenic viruses, and it has actually been used on the field to conduct the experimental campaign on a novel type of COVID-19 virus detector [25], providing excellent resolution and fast acquisition times compared with the several minutes it takes for the biological sensing element to react to the agent and stabilize.

Acknowledgment

The authors thank Alice Romagnoli, New York-Marche Structural Biology Center (NY-MaSBiC), Università Politecnica delle Marche, Ancona, Italy, for testing the device on-field and providing measures of the biological samples.

References

[1] L. Syedmoradi, A. Ahmadi, M. L. Norton, and K. Omidfar, "A review on nanomaterial-based field effect transistor technology for biomarker detection," *Microchimica Acta*, vol. 186, no. 11, pp. 1–23, Nov. 2019.

[2] H. Ehtesabi, "Application of carbon nanomaterials in human virus detection," *J. Sci., Adv. Mater. Devices*, vol. 5, no. 4, pp. 436–450, Dec. 2020.

[3] N. Gao et al., "Specific detection of biomolecules in physiological solutions using graphene transistor biosensors," *Proc. Nat. Acad. Sci. USA*, vol. 113, no. 51, pp. 14633–14638, Dec. 2016.

[4] E. W. Hill, A. Vijayaragahvan, and K. Novoselov, "Graphene sensors," *IEEE Sensors J.*, vol. 11, no. 12, pp. 3161–3170, Dec. 2011.

[5] A. Hlali and H. Zairi, "Graphene based-sensor for basal cell carcinoma detection," *IEEE Sensors J.*, vol. 21, no. 18, pp. 19930–19937, Sep. 2021.

[6] S. Wang et al., "Graphene field-effect transistor biosensor for detection of biotin with ultrahigh sensitivity and specificity," *Biosensors Bioelectron.*, vol. 165, Oct. 2020, Art. no. 112363.

[7] Y. Ohno, K. Maehashi, and K. Matsumoto, "Graphene field-effect transistors for label-free biological sensors," in *Proc. IEEE Sensors*, Nov. 2010, pp. 903–906.

[8] D. K. H. Tsang et al., "Chemically functionalised graphene FET biosensor for the label-free sensing of exosomes," *Sci. Rep.*, vol. 9, no. 1, pp. 1–10, Sep. 2019.

[9] C. Zheng, L. Huang, H. Zhang, Z. Sun, Z. Zhang, and G.-J. Zhang, "Fabrication of ultrasensitive field-effect transistor DNA biosensors by a directional transfer technique based on CVD-grown graphene," *ACS Appl. Mater. Interfaces*, vol. 7, no. 31, pp. 16953–16959, Aug. 2015.

[10] F. Yan, M. Zhang, and J. Li, "Solution-gated graphene transistors for chemical and biological sensors," *Adv. Healthcare Mater.*, vol. 3, no. 3, pp. 313–331, Mar. 2014.

[11] C. Reiner-Rozman, M. Larisika, C. Nowak, and W. Knoll, "Graphene-based liquid-gated field effect transistor for biosensing: Theory and experiments," *Biosensors Bioelectron.*, vol. 70, pp. 21–27, Aug. 2015.

[12] M. Pumera, "Graphene in biosensing," *Mater. Today*, vol. 14, nos. 7–8, pp. 308–315, Jul./Aug. 2011.

[13] G. Palazzo et al., "Detection beyond Debye's length with an electrolyte-gated organic field-effect transistor," *Adv. Mater.*, vol. 27, no. 5, pp. 911–916, Feb. 2015.

[14] D. Han, R. Chand, and Y.-S. Kim, "Microscale loop-mediated isothermal amplification of viral DNA with real-time monitoring on solution-gated graphene FET microchip," *Biosensors Bioelectron.*, vol. 93, pp. 220–225, Jul. 2017.

[15] X. Dong, Y. Shi, W. Huang, P. Chen, and L.-J. Li, "Electrical detection of DNA hybridization with single-base specificity using transistors based on CVD-grown graphene sheets," *Adv. Mater.*, vol. 22, no. 14, pp. 1649–1653, Apr. 2010.

[16] F. Chen, Q. Qing, J. Xia, and N. Tao, "Graphene field-effect transistors: Electrochemical gating, interfacial capacitance, and biosensing applications," *Chem.-Asian J.*, vol. 5, no. 10, pp. 2144–2153, Aug. 2010.

[17] X. Tan et al., "Ultrasensitive and selective bacteria sensors based on functionalized graphene transistors," *IEEE Sensors J.*, vol. 22, no. 6, pp. 5514–5520, Mar. 2022.

[18] M. Salehirozveh, P. Dehghani, M. Zimmermann, V. A. L. Roy, and H. Heidari, "Graphene field effect transistor biosensors based on aptamer for amyloid-β detection," *IEEE Sensors J.*, vol. 20, no. 21, pp. 12488–12494, Nov. 2020.

[19] D. Sadighbayan, A. Minhas-Khan, and E. Ghafar-Zadeh, "Laser-induced graphene-functionalized field-effect transistor-based biosensing: A potent candidate for COVID-19 detection," *IEEE Trans. Nanobiosci.*, vol. 21, no. 2, pp. 232–245, Apr. 2022.

[20] G. Seo et al., "Rapid detection of COVID-19 causative virus (SARS-CoV-2) in human nasopharyngeal swab specimens using field-effect transistor-based biosensor," *ACS Nano*, vol. 14, no. 4, pp. 5135–5142, Apr. 2020.

[21] R. R. X. Lim and A. Bonanni, "The potential of electrochemistry for the detection of coronavirus-induced infections," *TrAC Trends Anal. Chem.*, vol. 133, Dec. 2020, Art. no. 116081.

[22] L. Xiang, Z. Wang, Z. Liu, S. E. Weigum, Q. Yu, and M. Y. Chen, "Inkjet-printed flexible biosensor based on graphene field effect transistor," *IEEE Sensors J.*, vol. 16, no. 23, pp. 8359–8364, Dec. 2016.

[23] R. M. Torrente-Rodríguez et al., "SARS-CoV-2 RapidPlex: A graphene-based multiplexed telemedicine platform for rapid and low-cost COVID-19 diagnosis and monitoring," *Matter*, vol. 3, no. 6, pp. 1981–1998, Dec. 2020.

[24] S. Damiati et al., "Flex printed circuit board implemented graphene-based DNA sensor for detection of SARS-CoV-2," *IEEE Sensors J.*, vol. 21, no. 12, pp. 13060–13067, Jun. 2021.

[25] A. Romagnoli et al., "SARS-CoV-2 multi-variant rapid detector based on graphene transistor functionalized with an engineered dimeric ACE2 receptor," *Nano Today*, vol. 48, Feb. 2023, Art. no. 101729.

[26] R. S. Selvarajan, A. A. Hamzah, and B. Y. Majlis, "Transfer characteristics of graphene based field effect transistor (GFET) for biosensing application," in *Proc. IEEE Regional Symp. Micro Nanoelectronics (RSM)*, Aug. 2017, pp. 88–91.

[27] M. D'Agostino et al., "SARS-CoV-2 multi-variant graphene biosensor based on engineered dimeric ACE2 receptor," *MedRxiv*, p. 38, Oct. 2021, doi: 10.1101/2021.10.02.21264210.
[28] L. Xu et al., "On-chip integrated graphene aptasensor with portable readout for fast and label-free COVID-19 detection in virus transport medium," *Sensors Diag.*, vol. 1, no. 4, pp. 719–730, 2022.

Giorgio Biagetti (Member, IEEE) received the Laurea (summa cum laude) degree in electronics engineering and the Ph.D. degree in electronics and telecommunications engineering from the Università Politecnica delle Marche, Ancona, Italy, in 2000 and 2004, respectively.

He is currently an Assistant Professor with the Università Politecnica delle Marche, teaching digital electronics. He has authored more than 90 scientific papers in peer-reviewed journals and conferences. His current research interests include analog, digital, and mixed-signal circuit design and simulation; embedded systems design; wireless systems and networks; and signal processing.

Paolo Crippa (Senior Member, IEEE) received the Laurea (summa cum laude) degree in electronics engineering from the Università degli Studi di Ancona, Ancona, Italy, in 1994, and the Ph.D. degree in electronics engineering from the Polytechnic University of Bari, Bari, Italy, in 1999.

He is an Associate Professor with the Department of Information Engineering, Università Politecnica delle Marche, Ancona, teaching courses of basic and power electronics. He has authored or coauthored more than 120 papers in international journals, edited books, and conference proceedings. His current research interests include micro and nanoelectronics, statistical integrated circuit design and device modeling, mixed-signal and RF circuit design, signal processing, and neural networks.

Dr. Crippa is a member of the Associazione Italiana di Elettrotecnica, Elettronica, Automazione, Informatica e Telecomunicazioni (AEIT). He is currently an Associate Editor of IEEE ACCESS and serves on the editorial board of several scientific journals. He was a Guest Editor of *Sensors* (MDPI) and *Mathematics* (MDPI). He joined the technical program committees and international program committees for more than 100 scientific conferences and workshops and served as a reviewer for many scientific journals and conferences in the field of electronics, signal processing, and computational intelligence.

Michele Alessandrini received the Laurea degree in electronic engineering from the Università di Ancona, Ancona, Italy, in 2001, and the Ph.D. degree in electronic engineering from the Università Politecnica delle Marche, Ancona, in 2004.

In 2008, he joined the Department of Information Engineering (DII), Università Politecnica delle Marche, as a Technical Employee. His current research interests include embedded systems, neural networks, and hardware and software development.

Daniele Di Marino received the Laurea degree in bioinformatics and the Ph.D. degree in cellular and molecular biology from the University of Rome "Tor Vergata," Rome, Italy, in 2006 and 2009, respectively.

He spent several years as a Postdoctoral Researcher and a Research Assistant in Belgium, USA, and Switzerland. Presently, he is an Associate Professor in molecular biology with the Department of Life and Environmental Science, Università Politecnica delle Marche, Ancona, Italy. He has authored more than 55 scientific articles in peer-reviewed journals. His current research interests include protein design, computational structural biology, molecular modeling, molecular biology, biosensors' development, and binding free energy calculations.

Open Access funding provided by 'Università Politecnica delle Marche' within the CRUI CARE Agreement